Direct Approach to Treatment of Contact in Numerical Manifold Method

Yongtao Yang[1] and Hong Zheng[2]

Abstract: The numerical manifold method (NMM) is suitable for the solution of both continuous and discontinuous problems in geotechnical engineering. In the conventional NMM, the contact between blocks is treated with the open-close iteration, which needs to fix or remove spurious springs between two blocks in contact and to assume properly the normal stiffness and the tangential stiffness (the penalty parameters). Unreasonable values of stiffness would result in numerical problems. To avoid the penalty parameters, contacts are treated in a direct way in which contact forces are primal variables. Numerical examples have confirmed the correctness and feasibility of the proposed procedure.
DOI: 10.1061/(ASCE)GM.1943-5622.0000714.

Author keywords: Numerical manifold methods (NMM); Mathematical cover; Physical cover; Contact; Penalty parameter; Direct approach; Lagrange multiplier method.

Introduction

Numerical methods are powerful for rock mechanics and engineering analysis. With the maturing of computing techniques, there has been a tremendous explosion in the development and use of numerical methods (Reddy 2004). Typical methods include finite-difference methods (Perrone and Kao 1975), FEMs (Zienkiewicz and Taylor 2000; Goodman and John 1977; Desai et al. 1984; Katona 1983), meshfree methods (Rabczuk and Belytschko 2004; Belytschko et al. 1996), boundary element methods (Beskos 1987, 1997), extended FEMs (XFEMs) (Dolbow and Belytschko 1999; Areias and Belytschko 2005), generalized FEMs (GFEM) (Strouboulis et al. 2000; Duarte et al. 2001), discrete-element methods (DEMs) (Cundall 1971), and FEM/DEM (Munjiza 2004). These methods can be classified into three groups (Jing 2003): continuum methods, discontinuum methods, and hybrid methods. FEM/DEM is a straightforward methodology that makes use of the respective advantages of both continuum and discontinuum methods (Munjiza 2004; Sun et al. 2013). The application of FEM/DEM in practical rock mechanics problems could be found in many journal papers and books (Ma et al. 2014; Barla et al. 2012; Munjiza 2004; Yan et al. 2016).

In 1991, Shi (1991) developed a continuum-discontinuum method named the numerical manifold method (NMM) for geotechnical engineering. One of the main attractive advantages of NMM over other numerical methods is its ability to simulate continuous and discontinuous problems in a unified manner. Having the same basis as the partition of unity method (Babuška and Melenk 1997), NMM is considered as the generalization of the discontinuous deformation analysis (DDA) (Shi 1988) that addresses the system of distinct rock blocks. Over the past decades, NMM has been extensively studied and used in various fields including p-adaptive (Chen et al. 1998), Kirchhoff's thin plate bending problems (Zheng et al. 2013), seepage problems (Zheng et al. 2015c), simulation of reinforcement of rock mass (Wei et al. 2016), and initiation and propagation of cracks (Zheng et al. 2014a, b, 2015b; Wong and Wu 2014; Zhang et al. 2010; Ning et al. 2011) in rock materials. Although various problems were solved by the NMM, the previous works are limited in two-dimensional (2D) problems. Because of the difficulties in developing a complete contact theory that governs the interaction of three-dimensional (3D) blocks, application of the 3D NMM (Jiang et al. 2009, 2010; He and Ma 2010; He et al. 2013, 2014) to solve engineering problems, however, is very limited. A comprehensive review on the development of the NMM can be found in Ma et al. (2010).

Because the object analyzed by the NMM is usually a system of blocks with a great deal of persistent or no persistent joints, the treatment of contact between blocks or joint plains is one of the main tasks of the NMM. In NMMs, inheriting from DDAs, the penalty method is adopted to deal with contact, and Coulomb's friction law is used to determine the contact states (He et al. 2014). The physical meaning of a penalty parameter is the stiffness of the contact spring. Two kinds of contact springs, normal contact springs and tangential contact springs, are fixed between the contact surfaces. In each time step, the so called "open-close" iterations in NMM (or DDA) can be considered as a process of repeatedly adding or removing contact springs.

In the penalty method, because the contact force is calculated according to the penetration distance, the penetration between blocks, albeit not allowed for a real situation, is inevitable if contact exists. Also, the penalty parameters in the penalty method, which are hard to determine, are vital in analyses. The value of penalty parameters has a strong influence on accuracy of the solutions. A penalty parameter with too small a value cannot enforce accurately the constraint condition and may result in an unacceptable penetration of one body into the other, and the overall response is distorted (Bao et al. 2014). On the other hand, a penalty parameter with too big a value may enforce accurately the constraint condition. However, for a computer with a finite number of digits, a penalty parameter with too big a value will make the coefficient matrix become ill-conditioned (Bao et al. 2014).

[1]Assistant Professor, State Key Laboratory of Geomechanics and Geotechnical Engineering, Institute of Rock and Soil Mechanics, Chinese Academy of Sciences, Wuhan 430071, China. E-mail: scuhhc@126.com

[2]Professor, Key Laboratory of Urban Security and Disaster Engineering, Ministry of Education, Beijing Univ. of Technology, Beijing 100124, China (corresponding author). E-mail: hzheng@whrsm.ac.cn

Note. This manuscript was submitted on August 10, 2015; approved on April 7, 2016; published online on August 8, 2016. Discussion period open until January 8, 2017; separate discussions must be submitted for individual papers. This paper is part of the ***International Journal of Geomechanics***, © ASCE, ISSN 1532-3641.

To avoid the introduction of the artificial springs, the Lagrange multiplier method, which considers the Lagrange multipliers as basic unknowns, can impose the constraint conditions exactly. It has been implemented in DDA and successfully simulated the dynamic process of the Tangshan earthquake (Cai et al. 2000). However, it should be pointed out that if too many inactive constraints are enforced during the open-close iteration, the process will be interrupted because the coefficient matrix is rank deficient (Jiang and Zheng 2011). Moreover, the coefficient matrix is unsymmetrical if any contact pair is in the slip state.

Aiming to combine the advantages of Lagrangian multiplier and penalty methods, the augmented Lagrangian method (ALM) was proposed to deal with contact problems (Lin et al. 1996; Simo and Laursen 1992; Stupkiewicz et al. 2010). Detailed implementation of the ALM for contact problems of DDA could be found in Bao et al. (2014). Despite the attractive advantages including high accurate solutions, low sensibility to penalty parameters, and no need to increase the number of unknowns, ALM requires an iterative process to obtain the convergent contact forces, which may be time-consuming if the contact state changes during the iteration.

In an effort to deal with the contact problems of DDA, Zheng and Jiang (2009) removed the penalty parameter and the open-close iteration by reformulating the DDA as a nonlinear mixed complementarity problem in which the contact conditions are expressed by the complementarity equations and no artificial penalty parameters are needed. Later, they expressed the contact conditions by linear complementarity equations (Zheng and Li 2015a), which significantly improves the solving efficiency, as compared with their early work in Zheng and Jiang (2009), yet it cannot be comparable with the conventional DDA. Recently, Zheng et al. (2016) proposed the dual form of DDA, called DDA-d, which completely discards the artificial springs and has an efficiency comparable with DDA. In principle, the method in Zheng et al. (2016) can be extended to NMM, but the solution efficiency would be sacrificed considerably because a great deal of computation time has to be spent on the inverse of numerous matrices of large dimensions.

In this study, to circumvent the introduction of penalty parameters, a new technique called direct approach for contact problems is proposed. Beyond the Lagrange multiplier method, the direct approach can directly solve out the tangential contact force as well as the normal contact force by directly solving a nonsymmetric system. To save memory storage space and improve the numerical properties, however, a symmetrization treatment can be easily implemented.

Brief Introduction to NMM

To solve in a unified manner continuous and discontinuous problems in geotechnique, NMM uses two cover systems: the mathematical cover (MC) and the physical cover (PC). In this section, the basic concept of NMM is briefly introduced; more details can be found in Shi (1991), Zheng and Xu (2014b), and Cai et al. (2013).

The MC is composed of a series of mathematical patches (MPs), Ω_i^m, $i = 1, \ldots,$ and n^m, where, n^m = number of all MPs. Different MPs can partially overlap each other. The only requirement for a MC is to be able to cover the entire problem region Ω. The introduction of a MC is to generate the partition of unity subordinate to the PC, which will be explained shortly.

Associated with each MP $\{\Omega_i^m\}$ is a weight function $w_i(\boldsymbol{r})$, $i = 1, \ldots,$ and n^m, where $\boldsymbol{r}$ = position vector, satisfying the following properties

$$w_i(\boldsymbol{r}) = 0, \text{ if } \boldsymbol{r} \notin \Omega_i^m \tag{1}$$

$$0 \le w_i(\boldsymbol{r}) \le 1, \text{ if } \boldsymbol{r} \in \Omega_i^m \tag{2}$$

$$\sum_{i=1}^{n^m} w_i(\boldsymbol{r}) = 1, \text{ if } \boldsymbol{r} \in \Omega \tag{3}$$

$\{w_i(\boldsymbol{r})\}$ is collectively called the partition of unity subordinate to the MC $\{\Omega_i^m\}$.

Illustrated in Fig. 1(a) is an example in which the problem domain Ω containing a bifurcation crack Γ with two crack tips is covered by three MPs, i.e., Ω_1^m is the bigger circle, Ω_2^m is the smaller circle, and Ω_3^m is the rectangle. By cutting all the MPs $\{\Omega_i^m\}_1^3$ with the components of Ω—namely the boundary, the material interface, and the crack—the physical patches (PPs) are obtained, as shown in Figs. 1(b–d). One MP Ω_i^m might be split into several smaller domains, Ω_{j-i}^p, $j = 1, \ldots,$ and n_i^p, where Ω_{j-i}^p is referred to as the jth PP generated from the MP Ω_i^m; and n_i^p is the number of all the PPs that are all from the same MP Ω_i^m. All the PPs $\{\Omega_{j-i}^p\}$, are collectively termed as the PC and accordingly match Ω exactly.

Each PP Ω_{j-i}^p contains the local geometric features of the problem domain and can be assigned other given information. For example, Ω_{2-2}^p contains the crack tip of crack Γ [see Fig. 1(c)]. According to the geometric and mechanical features of Ω_{j-i}^p, one can construct a good enough local approximation $\boldsymbol{u}_{j-i}(\boldsymbol{r})$ over Ω_{j-i}^p to reflect the known information of the solution. $\boldsymbol{u}_{j-i}(\boldsymbol{r})$ could be expressed as

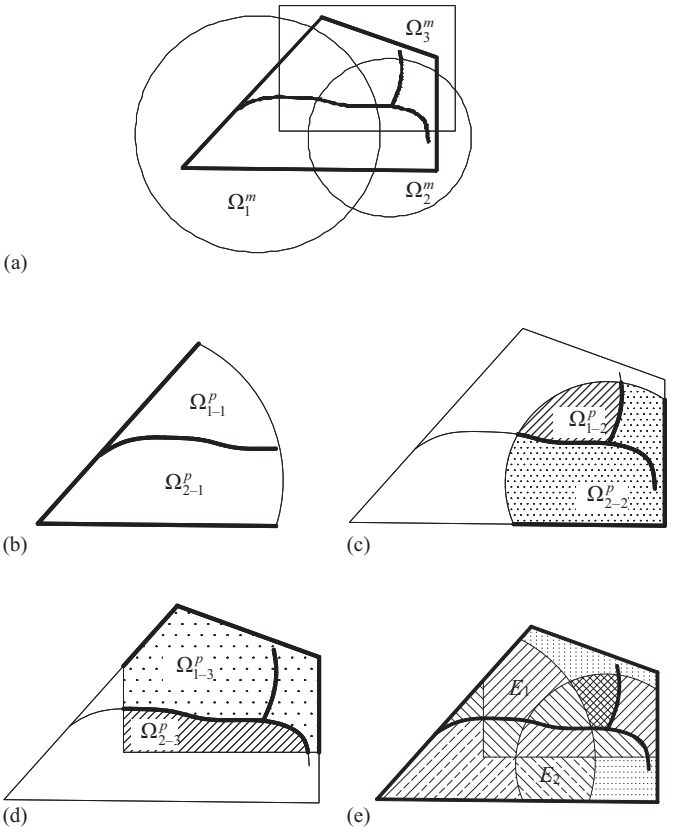

Fig. 1. Generation of manifold elements: (a) problem domain and MC; (b) two PPs from Ω_1^m; (c) two PPs from Ω_2^m; (d) two PPs from Ω_3^m; (e) manifold elements from the PC

$$\boldsymbol{u}_{j-i}(\boldsymbol{r}) = \boldsymbol{T}_{j-i}(\boldsymbol{r})\boldsymbol{d}_{j-i},\ \boldsymbol{r} \in \Omega^p_{j-i} \tag{4}$$

where vector $\boldsymbol{d}_{j-i}$ is composed of the degrees of freedom for PP Ω^p_{j-i}; and $\boldsymbol{T}_{j-i}(\boldsymbol{r})$ is composed of some given functions that could reflect the local behaviors of the solution over Ω^p_{j-i} (see details in Zheng and Xu 2014b).

By restricting $w_i(\boldsymbol{r})$ defined on Ω^m_i onto Ω^p_{j-i}, $j = 1, \ldots,$ and n^p_i, the weight function $w_{j-i}(\boldsymbol{r})$ subordinate to Ω^p_{j-i} is obtained. $w_{j-i}(\boldsymbol{r})$, $j = 1, \ldots, n^p_i$, might have the same expression as $w_i(\boldsymbol{r})$, but they have totally different definition domains, Ω^p_{j-i}, $j = 1, \ldots,$ and n^p_i, which are all from the same MP Ω^m_i. In addition, the local approximation $\boldsymbol{u}_{j-i}(\boldsymbol{r})$ is defined over Ω^p_{j-i}, totally independent of $\boldsymbol{u}_{k-i}(\boldsymbol{r})$ over Ω^p_{k-i}, which is adjacent to Ω^p_{j-i} and also from Ω^m_i. This enables NMM to simulate the solution jump across a discontinuity.

For simplicity of exposition, all Ω^p_{j-i}, $w_{j-i}(\boldsymbol{r})$, and $\boldsymbol{u}_{j-i}(\boldsymbol{r})$ are coded with a single subscript and represented by Ω^p_k, $w_k(\boldsymbol{r})$ and $\boldsymbol{u}_k(\boldsymbol{r})$, $k = 1, \ldots,$ and n^p, respectively. Here, n^p is the number of all the PPs, equal to

$$n^p = \sum_{i=1}^{n^m} n^p_i$$

In the conventional NMM, a manifold element, denoted by E_i, is a common domain of several neighboring PPs, which can serve as a basic unit in integrating the weak form of the problem. Fig. 1(e) displays all of the 12 numerical manifold elements generated from the MC shown in Fig. 1(a). Then, the global approximation $\boldsymbol{u}(\boldsymbol{r})$ in a manifold element E_i could be obtained by adding all the local approximations multiplied by the weight functions

$$\boldsymbol{u}(\boldsymbol{r}) = \sum_{k=1}^{n^p} w_k(\boldsymbol{r})\boldsymbol{u}_k(\boldsymbol{r}),\ \boldsymbol{r} \in E_i \tag{5}$$

Equations of Momentum Conservation of Block System

Contact Pair Analysis

Like DDA, NMM essentially reduces contact between blocks to angle-edge contact. The contact force analysis for a typical angle-edge contact is shown in Fig. 2. A vertex V of a master block Ω^m is in contact with an edge of a slave block Ω^s. The projection point of vertex V on slave block Ω^s is point V'. Unknown contact force, a point load $\boldsymbol{p}^V_g$, is acting at vertex V, and $-\boldsymbol{p}^V_g$ is acting on an edge of the slave block Ω^s. Point load $\boldsymbol{p}^V_g$ has the following decomposition

$$\boldsymbol{p}^V_g = p^V_n\boldsymbol{n} + p^V_s\boldsymbol{s} = \boldsymbol{L}_V\boldsymbol{p}^V \tag{6}$$

$$\boldsymbol{p}^V_g = (p^V_x, p^V_y)^{\mathrm{T}} \tag{7}$$

$$\boldsymbol{L}_V = [\boldsymbol{n}\ \boldsymbol{s}] \tag{8}$$

where $\boldsymbol{n}$ = exterior unit normal vector of Ω^s; $\boldsymbol{s}$ is perpendicular to $\boldsymbol{n}$ but along the counterclockwise boundary of Ω^s; and p^V_n and p^V_s are components of $\boldsymbol{p}^V_g$ along $\boldsymbol{n}$ and $\boldsymbol{s}$, respectively. Also, p^V_x and p^V_y are components of $\boldsymbol{p}^V_g$ along the x- and y- axis direction of the global coordinate system, respectively.

The normal relative distance g^n_V between V and V', at the end of a time step, can be obtained by the following formula:

$$g^n_V = \boldsymbol{n}^{\mathrm{T}}(\boldsymbol{x}_V - \boldsymbol{x}_{V'}) = \boldsymbol{n}^{\mathrm{T}}(\boldsymbol{x}^0_V - \boldsymbol{x}^0_{V'} + \boldsymbol{u}_V - \boldsymbol{u}_{V'}) \tag{9}$$

and the tangential relative displacement g^s_V, at the end of a time step, can be obtained by

$$g^s_V = \boldsymbol{s}^{\mathrm{T}}(\boldsymbol{u}_V - \boldsymbol{u}_{V'}) \tag{10}$$

where $\boldsymbol{x}^0_V$ and $\boldsymbol{x}_V$ are the coordinates of V, at the start and end of this time step, respectively; $\boldsymbol{x}^0_{V'}$ and $\boldsymbol{x}_{V'}$ are the coordinates of V', at the start and end of this time step, respectively; and $\boldsymbol{u}_V$ and $\boldsymbol{u}_{V'}$ are the incremental displacement of V and V' during this time step, respectively.

At the end of this time step, there are two possible contact states. For the first case, no contact occurs between the two blocks

$$g^n_V > 0$$

For the second case, the two blocks are in contact

$$g^n_V \le 0$$

Force Analysis and Control Equations for a Single Block

Considering a typical block Ω_i, as shown in Fig. 3(a), the external forces acting on it include the following:

1. Unknown contact force $\boldsymbol{p}^V_g$ is a point load that can be divided into two types:

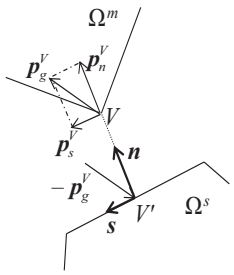

Fig. 2. Contact force analysis for a typical angle-edge contact

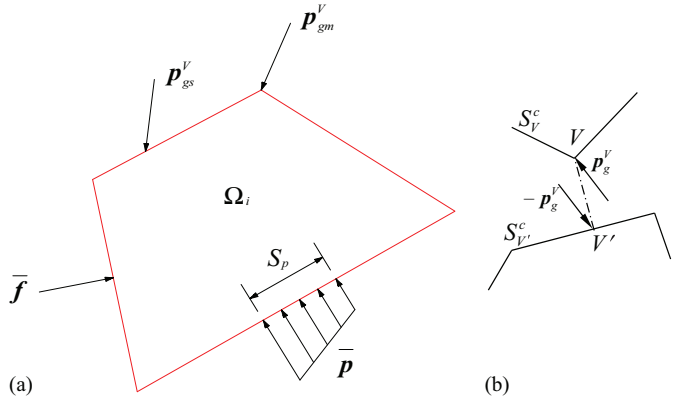

Fig. 3. Force analysis for a (a) single block and (b) contact pair

a. Master contact force $\boldsymbol{p}_{\mathrm{gm}}^{V}$ (equivalent to $\boldsymbol{p}_{g}^{V}$ in Fig. 2) acted at a vertex of block Ω_i.
b. Slave contact force $\boldsymbol{p}_{\mathrm{gs}}^{V}$ (equivalent to $-\boldsymbol{p}_{g}^{V}$ in Fig. 2) acted on an edge of block Ω_i.

2. Known surface traction $\bar{\boldsymbol{p}}$ acted on the boundary segment S_p of block Ω_i.
3. Known point load $\bar{\boldsymbol{f}}$ acted at some point of boundary of Ω_i.
4. Unknown volume load $\bar{\boldsymbol{b}} - \bar{\rho}\ddot{\boldsymbol{u}}$, where $\bar{\boldsymbol{b}}$ = volume force; $\bar{\rho}$ = density; and $\ddot{\boldsymbol{u}}$ = acceleration.

The control equations are classified as

1. Equation of motion

$$\partial\boldsymbol{\sigma} + \bar{\boldsymbol{b}} = \bar{\rho}\ddot{\boldsymbol{u}} \text{ , in } \Omega_i \tag{11}$$

with $\boldsymbol{\sigma}^{\mathrm{T}} = (\sigma_x, \sigma_y, \tau_{xy})$

2. Stress boundary

$$\partial_n\boldsymbol{\sigma} = \bar{\boldsymbol{p}} \text{ , on } S_p \tag{12}$$

with

$$\partial_n = \begin{bmatrix} n_x & 0 & n_y \\ 0 & n_y & n_x \end{bmatrix}$$

3. Force equilibrium conditions of contact surface [shown in Fig. 3(b)]

$$\begin{aligned} \partial_n\boldsymbol{\sigma} &= \textstyle\sum_V \delta_V(\boldsymbol{x})\boldsymbol{p}_g^V, \quad V \in S_V^c; \\ \partial_n\boldsymbol{\sigma} &= -\textstyle\sum_V \delta_{V'}(\boldsymbol{x})\boldsymbol{p}_g^V, \quad V' \in S_{V'}^c \end{aligned} \tag{13}$$

where $\delta_V(\boldsymbol{x})$ and $\delta_{V'}(\boldsymbol{x})$ are the Dirac delta function along boundaries S_V^c and $S_{V'}^c$ with the singularity at points V and V', respectively, because contacts are represented in NMM by point forces.

Equations of Momentum Conservation of Block System in Discrete Form

First, for the block system at the end of a time step, the weak form of momentum conservation is expressed as

$$\begin{aligned} \int_\Omega (\delta\boldsymbol{\varepsilon})^{\mathrm{T}}\boldsymbol{\sigma}d\Omega = \int_\Omega (\delta\boldsymbol{u})^{\mathrm{T}}(\bar{\boldsymbol{b}} - \bar{\rho}\ddot{\boldsymbol{u}})d\Omega + \int_{S_p}(\delta\boldsymbol{u})^{\mathrm{T}}\bar{\boldsymbol{p}}d\Omega \\ + \sum (\delta\boldsymbol{u})^{\mathrm{T}}\bar{\boldsymbol{f}} + \sum_V (\delta\boldsymbol{u}_V - \delta\boldsymbol{u}_{V'})\boldsymbol{p}_g^V \end{aligned} \tag{14}$$

where $\boldsymbol{u}$ is the incremental displacement vector; $\delta\boldsymbol{u}$ is the virtual displacement vector; and $\delta\boldsymbol{\varepsilon}$ is the virtual strain vector.

The incremental displacement vector $\boldsymbol{u}$ can be calculated by

$$\boldsymbol{u} = \boldsymbol{N}\boldsymbol{d} \tag{15}$$

where $\boldsymbol{N}$ and $\boldsymbol{d}$ = shape function matrix and generalized vector of freedom degrees, respectively.

Strain vector $\boldsymbol{\varepsilon}$ can be calculated by

$$\boldsymbol{\varepsilon} = \boldsymbol{L}_d\boldsymbol{u} = (\boldsymbol{L}_d\boldsymbol{N})\boldsymbol{d} = \boldsymbol{B}\boldsymbol{d} \tag{16}$$

where

$$\boldsymbol{L}_d = \begin{bmatrix} \dfrac{\partial}{\partial x} & 0 & \dfrac{\partial}{\partial y} \\ 0 & \dfrac{\partial}{\partial y} & \dfrac{\partial}{\partial x} \end{bmatrix}^{\mathrm{T}} \tag{17}$$

Stress vector $\boldsymbol{\sigma}$ can be expressed by strain vector $\boldsymbol{\varepsilon}$ through the constitutive relation

$$\boldsymbol{\sigma} = \boldsymbol{D}\boldsymbol{\varepsilon} + \boldsymbol{\sigma}_0 \tag{18}$$

where $\boldsymbol{\sigma}_0^{\mathrm{T}} = (\sigma_x^0\ \sigma_y^0\ \tau_{\mathrm{xy}}^0)$ is the initial stress vector; and $\boldsymbol{D}$ is the elastic matrix with

$$\boldsymbol{D} = \frac{E}{1-\nu^2}\begin{bmatrix} 1 & \nu & 0 \\ \nu & 1 & 0 \\ 0 & 0 & (1-\nu)/2 \end{bmatrix} \tag{19}$$

for the plane stress problem

$$\boldsymbol{D} = \frac{E(1-\nu)}{(1+\nu)(1-2\nu)}\begin{bmatrix} 1 & \dfrac{\nu}{(1-\nu)} & 0 \\ \dfrac{\nu}{(1-\nu)} & 1 & 0 \\ 0 & 0 & (1-2\nu)/[2(1-\nu)] \end{bmatrix} \tag{20}$$

for the plane strain problem.

Substituting Eqs. (15)–(18) into Eq. (14), the global system of equations can be written as

$$\boldsymbol{M}\ddot{\boldsymbol{d}} + \boldsymbol{E}\boldsymbol{d} - \boldsymbol{C}^{\mathrm{T}}\boldsymbol{p} = \boldsymbol{f}_0 + \boldsymbol{q}_0 \tag{21}$$

where $\boldsymbol{M}$ denotes the mass matrix

$$\boldsymbol{M} = \int_\Omega \bar{\rho}\boldsymbol{N}^{\mathrm{T}}\boldsymbol{N}d\Omega \tag{22}$$

$\boldsymbol{E}$ denotes the stiffness matrix

$$\boldsymbol{E} = \int_\Omega \boldsymbol{B}^{\mathrm{T}}\boldsymbol{D}\boldsymbol{B}d\Omega \tag{23}$$

$\boldsymbol{C}$ denotes contact matrix

$$\boldsymbol{C}^{\mathrm{T}} = [\boldsymbol{C}_{V_1}^{\mathrm{T}}, \cdots, \boldsymbol{C}_{V_c}^{\mathrm{T}}] \tag{24}$$

in which subscript c is the number of contact pairs

$$\boldsymbol{C}_{V_i} = \boldsymbol{L}_{V_i}^{\mathrm{T}}(\boldsymbol{N}_{V_i} - \boldsymbol{N}_{V_i'}) \tag{25}$$

The contact force vector is defined in the local coordinate system of contact edge, expressed as

$$\boldsymbol{p}^{\mathrm{T}} = [p_n^{V_1}, p_s^{V_1}, \cdots, p_n^{V_c}, {}_{p}^{sV_c}] \tag{26}$$

$$\boldsymbol{p}_{V_i} = [p_n^{V_i}, p_s^{V_i}]^{\mathrm{T}} \tag{27}$$

The global force vector can be written as

$$\boldsymbol{f}_0 = \int_\Omega \boldsymbol{N}^{\mathrm{T}}\bar{\boldsymbol{b}}d\Omega + \int_{S_p} \boldsymbol{N}^{\mathrm{T}}\bar{\boldsymbol{p}}\mathrm{dS} + \sum \boldsymbol{N}^{\mathrm{T}}\bar{\boldsymbol{f}} \tag{28a}$$

and

$$\boldsymbol{q}_0 = -\int_\Omega \boldsymbol{B}^{\mathrm{T}}\boldsymbol{\sigma}_0 d\Omega \tag{28b}$$

There are two ways to solve Eq. (21), namely, the direct integration method and the modal superposition method (Yang et al. 2014). In the present work, the Newmark direct integration method is adopted.

According to the Newmark integration scheme of constant acceleration, at time $t = t_0 + \Delta t$, with t_0 a selected initial time and Δt the time elapsed, $\boldsymbol{d}$ can be calculated by

$$\boldsymbol{d} = \dot{\boldsymbol{d}}_0 \Delta t + \frac{\Delta t^2}{2} \ddot{\boldsymbol{d}} \tag{29}$$

with $\dot{\boldsymbol{d}}_0$ = initial time change rate of $\boldsymbol{d}$. It is noticed that more sophisticated Newmark integration schemes can be found in Jiang et al. (2009).

Solving Eq. (29) for $\ddot{\boldsymbol{d}}$ leads to

$$\ddot{\boldsymbol{d}} = \frac{2}{\Delta t^2} \boldsymbol{d} - \frac{2}{\Delta t} \dot{\boldsymbol{d}}_0 \tag{30}$$

Substituting Eq. (30) into Eq. (21) yields

$$\boldsymbol{K}_0 \boldsymbol{d} - \boldsymbol{C}^{\mathrm{T}} \boldsymbol{p} = \tilde{\boldsymbol{f}}_0 \tag{31}$$

in which the generalized stiffness matrix $\boldsymbol{K}_0$ and generalized load vector $\tilde{\boldsymbol{f}}_0$ are defined as

$$\boldsymbol{K}_0 = \frac{2}{\Delta t^2} \boldsymbol{M} + \boldsymbol{E} \tag{32}$$

and

$$\tilde{\boldsymbol{f}}_0 = \boldsymbol{f}_0 + \boldsymbol{q}_0 + \frac{2}{\Delta t} \boldsymbol{M} \dot{\boldsymbol{d}}_0 \tag{33}$$

respectively.

Once $\boldsymbol{d}$ is obtained, $\ddot{\boldsymbol{d}}$ can be calculated immediately; then the time change rate of $\boldsymbol{d}$ is computed by

$$\dot{\boldsymbol{d}} = \dot{\boldsymbol{d}}_0 + \ddot{\boldsymbol{d}} \Delta t$$

which will be the initial time change rate of next Δt.

As in DDA, the time integration used by both the conventional NMM and the present direct approach contain inherent algorithm damping, which is dependent on the size of the time step (Doolin and Sitar 2004). Therefore, the time step size has an important influence on the accuracy and convergence rate of the numerical solution (Jiang et al. 2013). Jiang et al. (2013) have studied the influence of time step on the accuracy of DDA in great detail and concluded that the algorithmic-damping ratio is proportional to the size of the time step. Because the mechanism of algorithm damping for both NMM and DDA are the same, the impact of the size of the time step on the solution precision will not be discussed in this paper.

Formulations of the Direct Approach

Contact Equations

To solve Eq. (31), $2c$ more equations named contact equations should be complemented, where c = number of contact pairs in the system. Because the contact detection technology in NMM is inherited from the DDA, the procedures for finding the contact pairs for NMM will not be discussed in this section. The contact state for a contact pair, at the end of a time step, should be among one of the three cases, namely, sticky state, slip state, and open state. Each contact state has two additional equations.

Sticky State

At the end of the time step, if the contact pair is in sticky state, the normal relative distance g_V^n between V and V', should satisfy

$$g_V^n = \boldsymbol{n}^{\mathrm{T}} (\boldsymbol{x}_V - \boldsymbol{x}_{V'}) = \boldsymbol{n}^{\mathrm{T}} (\boldsymbol{N}_V - \boldsymbol{N}_{V'}) \boldsymbol{d} + g_n^0 = 0 \tag{34}$$

with

$$g_n^0 = \boldsymbol{n}^{\mathrm{T}} (\boldsymbol{x}_V^0 - \boldsymbol{x}_{V'}^0) \tag{35}$$

being the initial normal gap of the contact pair.

The tangential relative displacement, g_V^s, defined by

$$g_V^s = \boldsymbol{s}^{\mathrm{T}} (\boldsymbol{N}_V - \boldsymbol{N}_{V'}) \boldsymbol{d} \tag{36}$$

is set at zero if the contact pair is not in the open state at the end of the last time step. However, if the contact pair is in the open state at the end of the last step, g_V^s is indeterminate after it becomes the sticky state. In this case, g_V^s is set as

$$g_V^s = \tilde{g}_V^s \tag{37}$$

where $\tilde{g}_V^s$ was determined when the open contact pair overlapped during a past iteration within this time step, reading

$$\tilde{g}_V^s = \frac{g_n^0}{g_n^0 - \bar{g}_n^V} \bar{g}_V^s \tag{38}$$

where $\bar{g}_V^n$ = the overlapping distance (negative); and $\bar{g}_V^s$ = tangential displacement, as shown in Fig. 4.

The displacement constraint equations of Eqs. (34)–(36) could be rewritten in matrix form

$$\boldsymbol{C}_V \boldsymbol{d} = \boldsymbol{g}_F \tag{39}$$

in which

$$\boldsymbol{C}_V = \boldsymbol{L}_V^{\mathrm{T}} (\boldsymbol{N}_V - \boldsymbol{N}_{V'}) \tag{40}$$

$$\boldsymbol{g}_F = \begin{pmatrix} -g_n^0 \\ \tilde{g}_V^s \end{pmatrix} \tag{41}$$

Slip State

At the end of this time step, if the contact pair is in slip state, the normal relative distance g_V^n between V and V' should satisfy

$$g_V^n = \boldsymbol{n}^{\mathrm{T}} (\boldsymbol{N}_V - \boldsymbol{N}_{V'}) \boldsymbol{d} + g_n^0 = 0 \tag{42}$$

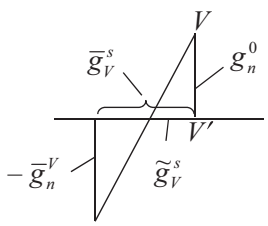

Fig. 4. Calculation diagram of $\tilde{g}_V^s$

the same as the sticky state, namely Eq. (34).

The tangential contact force should satisfy the Colombian friction law, that is

$$p_s^V = -\mu \text{sign}(g_V^s) p_n^V \tag{43}$$

Although Eq. (43) can serve as a constraint in the direct approach, and p_s^V can be directly solved out, to keep symmetry of the system matrix, nevertheless, Eq. (43) is replaced with the following form

$$p_s^V = \mu \text{sign}(\bar{p}_s^V) \bar{p}_n^V \tag{44}$$

where $\bar{p}_s^V$ and $\bar{p}_n^V$ = normal and tangential contact forces of last iteration (sticky state or slip state), respectively; and μ denotes friction factor.

The replacement of Eq. (43) by Eq. (44) is justified because the equilibrium in the normal direction has actually been reached at the end of the last iteration, that is, the normal contact force p_n^V has been calculated exact enough at the end of the last iteration. Katona (1983) used such a replacement to make a symmetric matrix, but in the framework of static analysis, as the author admitted, the symmetrization sacrifices convergence. Later, therefore, Zheng et al. (2004) gave up this replacement; instead, the authors proposed to directly use Eq. (43) and a new decision matrix. In the framework of dynamic analysis, the open-close iteration is always convergent due to the introduction of inertia matrices. As a result, here the symmetrization is still adopted, with little impact to convergence.

As an aside, if the Lagrange multiple method is used, the tangential contact force p_s^V cannot be solved out directly, and Eq. (44) is compulsory.

Based on the previous description, only one additional displacement constraint equation is needed for the slip state

$$\boldsymbol{C}_V^n \boldsymbol{d} = -g_n^0 \tag{45}$$

where $\boldsymbol{C}_V^n$ is the first line of $\boldsymbol{C}_V$ defined in Eq. (40), namely

$$\boldsymbol{C}_V^n = \boldsymbol{n}^{\mathrm{T}} (\boldsymbol{N}_V - \boldsymbol{N}_{V'}) \tag{46}$$

In this case, cross out the column elements of $\boldsymbol{C}^{\mathrm{T}}$ related to p_s^V and superpose initial stress vector $\boldsymbol{q}_0$ with $-p_s^V (\boldsymbol{C}_V^s)^{\mathrm{T}}$, where $\boldsymbol{C}_V^s$ is the second row of $\boldsymbol{C}_V$, that is

$$\boldsymbol{C}_V^s = \boldsymbol{s}^{\mathrm{T}} (\boldsymbol{N}_V - \boldsymbol{N}_{V'}) \tag{47}$$

Open State

At the end of this time step, if the contact pair is in the open state, the values of normal and tangential contact forces both vanish, leading to

$$p_n^V = 0 \tag{48}$$

$$p_s^V = 0 \tag{49}$$

For this case, no additional equations are needed, only the two column elements of $\boldsymbol{C}^{\mathrm{T}}$ related to p_n^V and p_s^V are needed to be crossed out.

Solving the System Equations

When contact states of all the contact pairs are given, the system matrix is finally rewritten as

$$\begin{bmatrix} \boldsymbol{K}_0 & \tilde{\boldsymbol{C}}^{\mathrm{T}} \\ \tilde{\boldsymbol{C}} & \boldsymbol{0} \end{bmatrix} \begin{pmatrix} \Delta \boldsymbol{d} \\ -\tilde{\boldsymbol{p}} \end{pmatrix} = \begin{pmatrix} \boldsymbol{f}_0 + \boldsymbol{f}_1 + \tilde{\boldsymbol{q}}_0 \\ \tilde{\boldsymbol{g}} \end{pmatrix} \tag{50}$$

To improve the property of the system matrix, Eq. (50) is scaled such that all variables have approximate magnitude order

$$\begin{bmatrix} \boldsymbol{K}_0 & \alpha \tilde{\boldsymbol{C}}^{\mathrm{T}} \\ \alpha \tilde{\boldsymbol{C}} & \boldsymbol{0} \end{bmatrix} \begin{pmatrix} \Delta \boldsymbol{d} \\ \tilde{\boldsymbol{p}}' \end{pmatrix} = \begin{pmatrix} \boldsymbol{f}_0 + \boldsymbol{f}_1 + \tilde{\boldsymbol{q}}_0 \\ \alpha \tilde{\boldsymbol{g}} \end{pmatrix} \tag{51}$$

where $\tilde{\boldsymbol{p}} = -\alpha \boldsymbol{p}'$, $\boldsymbol{q}0 = \boldsymbol{q}_0 - p_s^V (\boldsymbol{C}_V^s)^{\mathrm{T}}$; and α is a parameter proportional to the diagonal elements of $\boldsymbol{K}_0$, and is set as $\sqrt{\boldsymbol{K}_{0\min} * \boldsymbol{K}_{0\max}}$ in this study, where $\boldsymbol{K}_{0\min}$ is the minimum value of the diagonal elements of $\boldsymbol{K}_0$, and $\boldsymbol{K}_{0\max}$ is the maximum value of the diagonal elements of $\boldsymbol{K}_0$. $\tilde{\boldsymbol{C}}$ and $\boldsymbol{g}$ are composed of $\boldsymbol{C}_V$ and $\boldsymbol{g}_F$ of all the contact pairs, respectively.

Obviously, Eq. (51) is a KKT equation. The detailed solving procedure for Eq. (51) could be found in Zheng and Li (2007).

It should be pointed out that after the contact detection is performed by the original NMM code, the redundant contact pairs might be picked out. These redundant contact pairs would not bring troubles to the penalty method–based procedures, because a redundant contact pair actually corresponds to fixing a redundant couple of normal and tangential contact springs. In the direct approach, however, a redundant contact pair might cause the coefficient matrix in Eq. (51) to be rank deficient. Consequently, after the contact pairs are picked out, those redundant contact pairs must be removed if the direct approach is used.

Contact State Update

During the open-close iteration process, the update of the contact state for each contact pair is determined by the state variables at the beginning and end of this iteration (Table 1). According to the contact state at the beginning of this iteration, three cases are divided, namely,

1. The contact state at the beginning of this iteration is in the sticky state (see Table 1). Check the state variables at the end of this iteration, if

Table 1. Update Mode of Contact State for Contact Pair during Open-Close Iteration

		i		
$i-1$	C & R	Sticky	Slip	Open
Sticky	Check	$p_n^V \geq 0$ and $\lvert p_s^V \rvert \leq [p_s^V]$	$p_n^V \geq 0$ and $\lvert p_s^V \rvert > [p_s^V]$	$p_n^V < 0$
	RS – i	$g_V^n = 0$	$g_V^n = 0$ with	$p_n^V = 0$
		g_V^s invariant	$p_s^V = \text{sign}(p_s^V)[p_s^V]$	$p_s^V = 0$
Slip	Check	$p_n^V \geq 0$ and $p_s^V g_V^s > 0$	$p_n^V \geq 0$ and $p_s^V g_V^s \leq 0$	$p_n^V < 0$
	RS – i	$g_V^n = 0$	$g_V^n = 0$ with	$p_n^V = 0$
		$g_V^s = 0$	$p_s^V = \text{sign}(p_s^V)[p_s^V]$	$p_s^V = 0$
Open	Check	$g_V^n < 0$ and $\lvert \tilde{g}_V^s \rvert < \lvert g_n^0 \rvert$	$g_V^n < 0$ and $\lvert \tilde{g}_V^s \rvert \geq \lvert g_n^0 \rvert$	$g_V^n \geq 0$
	RS – i	$g_V^n = 0$	$g_V^n = 0$ with	$p_n^V = 0$
		$g_V^s = \tilde{g}_V^s$	$p_s^V = f_j$	$p_s^V = 0$

Note: $i-1$ and $i = (i-1)$th and the ith iteration, respectively; RS – i = the right-side items in the contact constraint conditions at the ith iteration; C & R = "Check the contact state followed by setting the right side items in the contact constraint conditions at the ith iteration."

a) Normal contact force $p_n^V \geq 0$ and the absolute value of tangential contact force p_s^V is less than or equal to the maximum frictional force, namely, $|p_s^V| \leq [p_s^V]$ ($[p_s^V] = f_j + \mu |p_n^V|$, where f_j denotes the contribution of cohesion), then the contact state at the end of this iteration is set to be sticky, the normal relative distance $g_V^n = 0$, and the tangential relative displacement g_V^s keeps invariant;
b) Normal contact force $p_n^V \geq 0$ and the absolute value of tangential contact force p_s^V is greater than the maximum frictional force, namely, $|p_s^V| > [p_s^V]$, then the contact state at the end of this iteration is set to be slip, the normal relative distance $g_V^n = 0$, and tangential contact force $p_s^V = \text{sign}(p_s^V)[p_s^V]$; and
c) Normal contact force $p_n^V < 0$, then the contact state at the end of this iteration is set to be open, normal contact force $p_n^V = 0$, and tangential contact force $p_s^V = 0$.

2. The contact state at the beginning of this iteration is in the slip state (Table 1), check the state variables at the end of this iteration, if
   a) Normal contact force $p_n^V \geq 0$, and tangential contact force p_s^V and tangential relative displacement g_V^s are in the same direction, namely, $p_s^V g_V^s > 0$, then the contact state at the end of this iteration is set to be sticky, the normal relative distance $g_V^n = 0$, and tangential relative displacement $g_V^s = 0$;
   b) Normal contact force $p_n^V \geq 0$, and tangential contact force p_s^V and tangential relative displacement g_V^s are in opposite direction, namely, $p_s^V g_V^s \leq 0$, then the contact state at the end of this iteration is set to be in the slip state, the normal relative distance $g_V^n = 0$, tangential contact force $p_s^V = \text{sign}(p_s^V)[p_s^V]$; and
   c) Normal contact force $p_n^V < 0$, then the contact state at the end of this iteration is set to be open, normal contact force $p_n^V = 0$, and tangential contact force $p_s^V = 0$.
3. The contact state at the beginning of this iteration is in the open state (Table 1), check the state variables at the end of this iteration, if
   a) Normal relative distance $g_V^n < 0$, calculate $\tilde{g}_V^s$ according Eq. (38); if $|\tilde{g}_V^s| < |g_n^0|$ (see Fig. 4 for the definition of $\tilde{g}_V^s$ and g_n^0), then the contact state at the end of this iteration is set to be sticky, the normal relative distance $g_V^n = 0$, and tangential relative displacement $g_V^s = \tilde{g}_V^s$;
   b) Normal relative distance $g_V^n < 0$, and $|\tilde{g}_V^s| \geq |g_n^0|$, then the contact state at the end of this iteration is set to be in the slip state, the normal relative distance $g_V^n = 0$, tangential contact force $p_s^V = f_j$; and
   c) Normal relative distance $g_V^n \geq 0$, then the contact state at the end of this iteration is set to be open, normal contact force $p_n^V = 0$, and tangential contact force $p_s^V = 0$.

Numerical Examples

Typical numerical tests with the present direct approach for contact problems in NMM were performed, and results were compared with those of the penalty method. The physical units used in the present work are based on the international standard unit system without specifying.

Momentum Conservation Test

On a rigid and frictionless slide, shown in Fig. 5, the left-side block (Block 1) with initial horizontal speed V_0, moves toward and finally collides with the right-side stationary block (Block 2). The parameters for Block 1 are listed as $V_0 = 1$, width $w = 2$, height $h = 2$, Young's modulus $E = 200 \times 10^9$, Poisson's ratio $\upsilon = 0.25$, and density $\rho = 1{,}000$. For Block 2, two cases are considered, namely, (1) the material and dimension parameters are the same as those of Block 1, as shown in Fig. 5(a); and (2) the parameters are listed as width $w = 1$, height $h = 1$, Young's modulus $E = 200 \times 10^9$, Poisson's ratio $\upsilon = 0.25$, and density $\rho = 2{,}000$, as shown in Fig. 5 (b). The bottom, left, and right sides of the slide are all fixed by stiff springs with stiffness of $100E$ in both horizontal and vertical directions. Theoretically, the block system should satisfy the law of horizontal momentum conservation. In other words, the global horizontal momentum should always be 4,000 even after Block 1 collides with Block 2.

Shown in Fig. 6 are the discrete models for this momentum conservation test. The time step length Δt and number of time steps are taken as 0.01 and 100, respectively. To study the influence of penalty parameter value p on accuracy of this contact problem, three cases, namely, NMM1 with $p = E$, NMM2 with $p = 10E$, and NMM3 with $p = 100E$, are considered for the purpose.

The total horizontal momentum, momentums of Blocks 1 and 2 versus time step, are plotted in Fig. 7. It is shown that the values of total horizontal momentum are almost identical to the theoretical values, which means the proposed direct approach could pass this momentum conversation test.

The values of momentum and velocity for Blocks 1 and 2 are also listed in Tables 2–5. It is shown that accuracy for the penalty method could be improved by increasing the value of the penalty parameter. However, as discussed in the previous section, penalty parameters that are too big will make the governing equations become ill-conditioned. Overall, accuracy of the proposed direct approach exceeds the penalty method with different values of the penalty parameter. Moreover, the proposed method is free from the penalty parameter, which is very difficult to be determined for different problems.

Sliding Problem

Using this classical example, accuracy of the present direct approach is compared with the penalty method with different values of the penalty parameter. Shown in Fig. 8 is a sliding rectangle block that is 2×1 m on a ramp with a slope angle of α. The

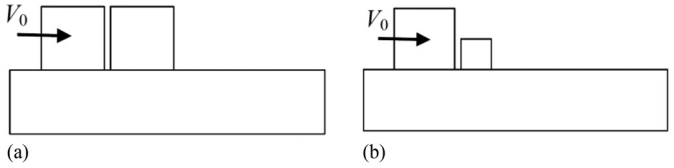

Fig. 5. Block 1 moves toward Block 2: (a) a big block collides with another big block; (b) a big block collides with another small block

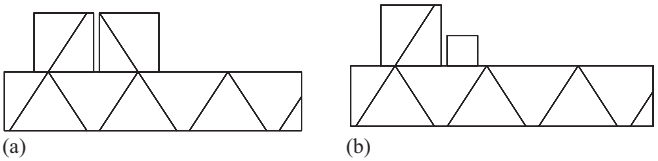

Fig. 6. Discrete models for the momentum conservation test: (a) a big block collides with another big block; (b) a big block collides with another small block

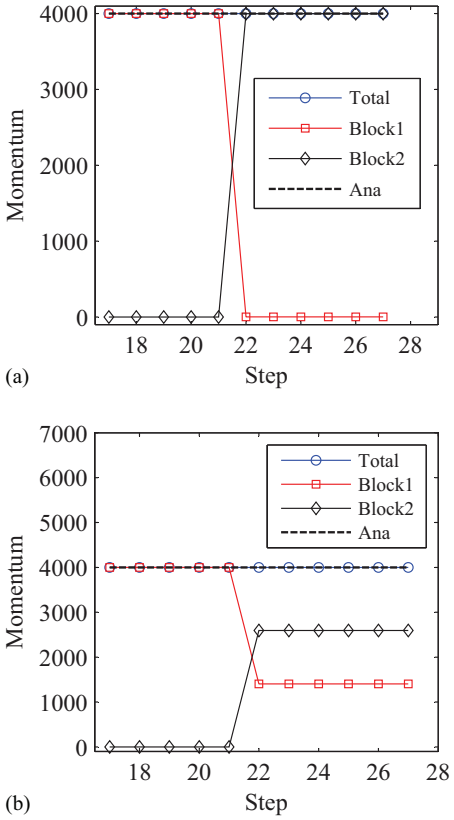

Fig. 7. Computed momentum versus time step: (a) a big block collides with another big block; (b) a big block collides with another small block

Table 2. Computed Momentum of the Two Blocks: A Big Block Collides with Another Big Block

	Before collision			After collision		
Methods	Block 1	Block 2	Total	Block 1	Block 2	Total
Direct approach	4000.000	0.000	4000.000	0.448	3999.552	4000.000
NMM1	4000.000	0.000	4000.000	0.848	3999.153	4000.001
NMM2	4000.000	0.000	4000.000	0.489	3999.511	4000.000
NMM3	4000.000	0.000	4000.000	0.453	3999.547	4000.000
Theoretical value	4000.000	0.000	4000.000	0.000	4000.000	4000.000

Table 3. Computed Velocity of the Two Blocks: A Big Block Collides with Another Big Block

	Before collision		After collision	
Methods	Block 1	Block 2	Block 1	Block 2
Direct approach	1.00000	0.00000	0.00011	0.99989
NMM1	1.00000	0.00000	0.00021	0.99979
NMM2	1.00000	0.00000	0.00012	0.99988
NMM3	1.00000	0.00000	0.00011	0.99989
Theoretical value	1.00000	0.00000	0.00000	1.00000

block and the ramp have the same material parameters: Young's modulus $E = 200$ MPa, Poisson's ratio $\upsilon = 0.25$, and density $\rho = 2{,}750\ \text{kg/m}^3$. The bottom and right sides of the ramp are all fixed

Table 4. Computed Momentum of the Two Blocks: A Big Block Collides with Another Small Block

	Before collision			After collision		
Methods	Block 1	Block 2	Total	Block 1	Block 2	Total
Direct approach	4000.000	0.000	4000.000	1405.311	2595.779	4001.088
NMM1	4000.000	0.000	4000.000	1406.104	2595.475	4001.579
NMM2	4000.000	0.000	4000.000	1405.921	2595.655	4001.576
NMM3	4000.000	0.000	4000.000	1405.313	2595.777	4001.088
Theoretical value	4000.000	0.000	4000.000	1333.333	2666.667	4000.000

Table 5. Computed Velocity of the Two Blocks: A Big Block Collides with Another Small Block

	Before collision		After collision	
Methods	Block 1	Block 2	Block 1	Block 2
Direct method	1.00000	0.00000	0.35133	1.29789
NMM1	1.00000	0.00000	0.35153	1.29774
NMM2	1.00000	0.00000	0.35148	1.29783
NMM3	1.00000	0.00000	0.35133	1.29789
Theoretical value	1.00000	0.00000	0.33333	1.33333

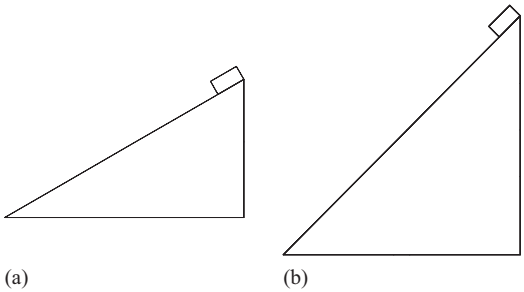

Fig. 8. Block slides along a ramp: (a) slope angle $\alpha = 30°$; (b) slope angle $\alpha = 45°$

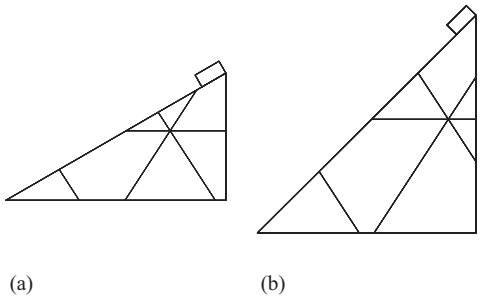

Fig. 9. Discrete models for the block and ramp: (a) slope angle $\alpha = 30°$; (b) slope angle $\alpha = 45°$

by stiff springs with stiffness of $100E$ in both horizontal and vertical directions.

It is easy to derive the exact sliding displacement of the block

$$s = \frac{1}{2}(\sin\alpha - \mu\cos\alpha)gt^2 \tag{52}$$

at time t (s); where s = sliding distance of the block center point (in meters); g = gravity speed (9.8 m/s^2); $\mu = \tan\varphi$; and φ the friction angle.

The discrete models with different slope angles for this problem are shown in Fig. 9. Let the time step length $\Delta t = 0.01$ s and total computation time = 2 s, with a set of combinations of slope angles and friction angles assumed. Fig. 10 displays the relative error distributions from the direct and penalty methods during sliding. From all these results, it is observed that the proposed direct approach is more accurate than the penalty method with different values of the penalty parameters.

Arch Dam Problem

In the design of an arch dam, the pure arch method is often used to analyze the stress state of the arch dam. The pure arch method assumes that the arch dam consists of a series of independent horizontal arches that will bear all the load acting on the dam, and each arch is simplified as an elastic arch whose end sides are fixed for calculation. Fig. 11 shows an arch dam with a layer of arch, and a point load $f = 1.5$ acts at the upstream side of the dam. The downstream side of the bedrock is fixed. The bedrock and the dam have the same material parameters: density $\rho = 0.3$, unit

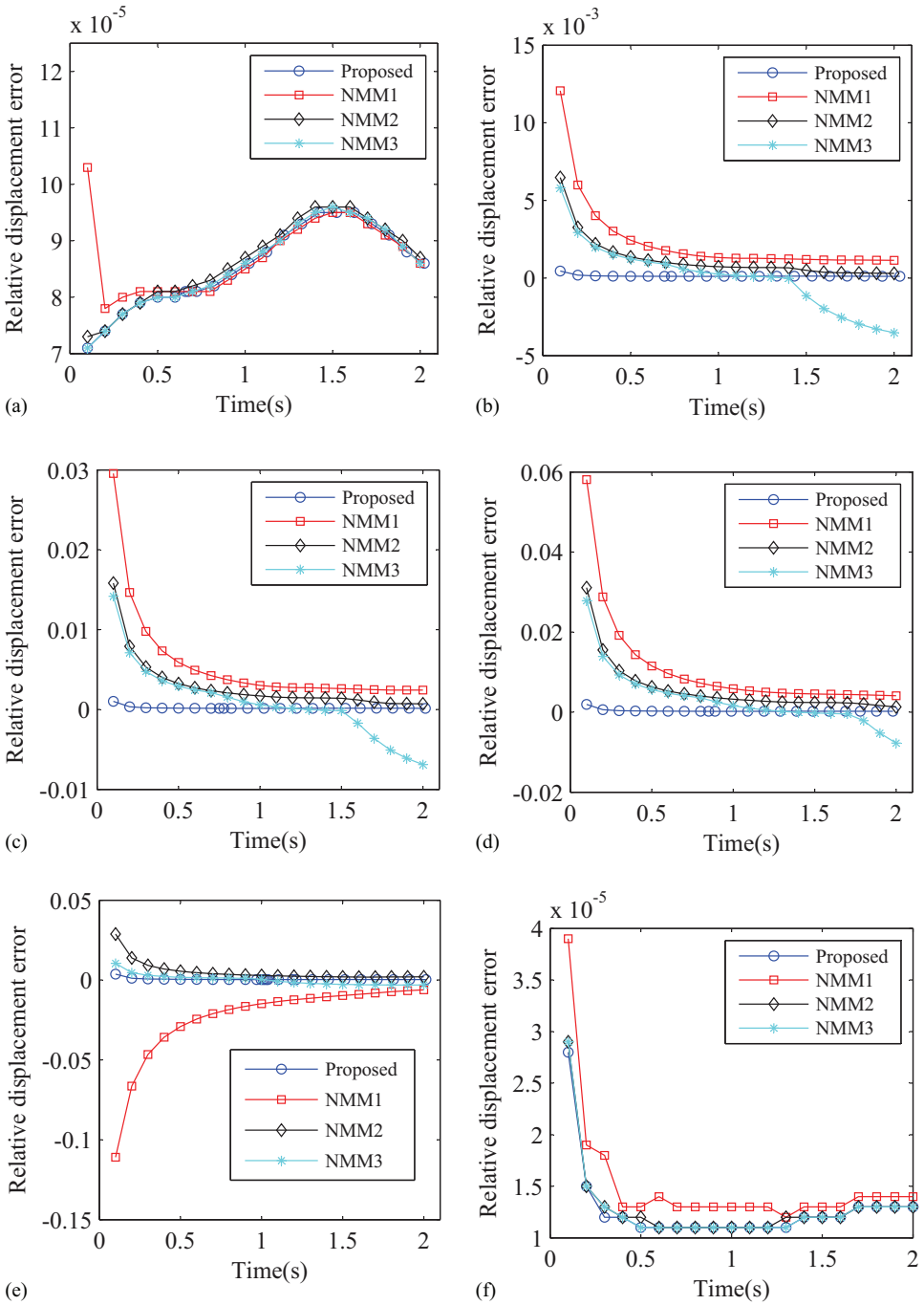

Fig. 10. Comparisons between the proposed direct method and penalty method under different slope angles α and friction angles φ: (a) $\alpha = 30°$, $\varphi = 0°$; (b) $\alpha = 30°$, $\varphi = 5°$; (c) $\alpha = 30°$, $\varphi = 10°$; (d) $\alpha = 30°$, $\varphi = 15°$; (e) $\alpha = 30°$, $\varphi = 20°$; (f) $\alpha = 45°$, $\varphi = 0°$; (g) $\alpha = 45°$, $\varphi = 5°$; (h) $\alpha = 45°$, $\varphi = 10°$; (i) $\alpha = 45°$, $\varphi = 15°$; (j) $\alpha = 45°$, $\varphi = 20°$

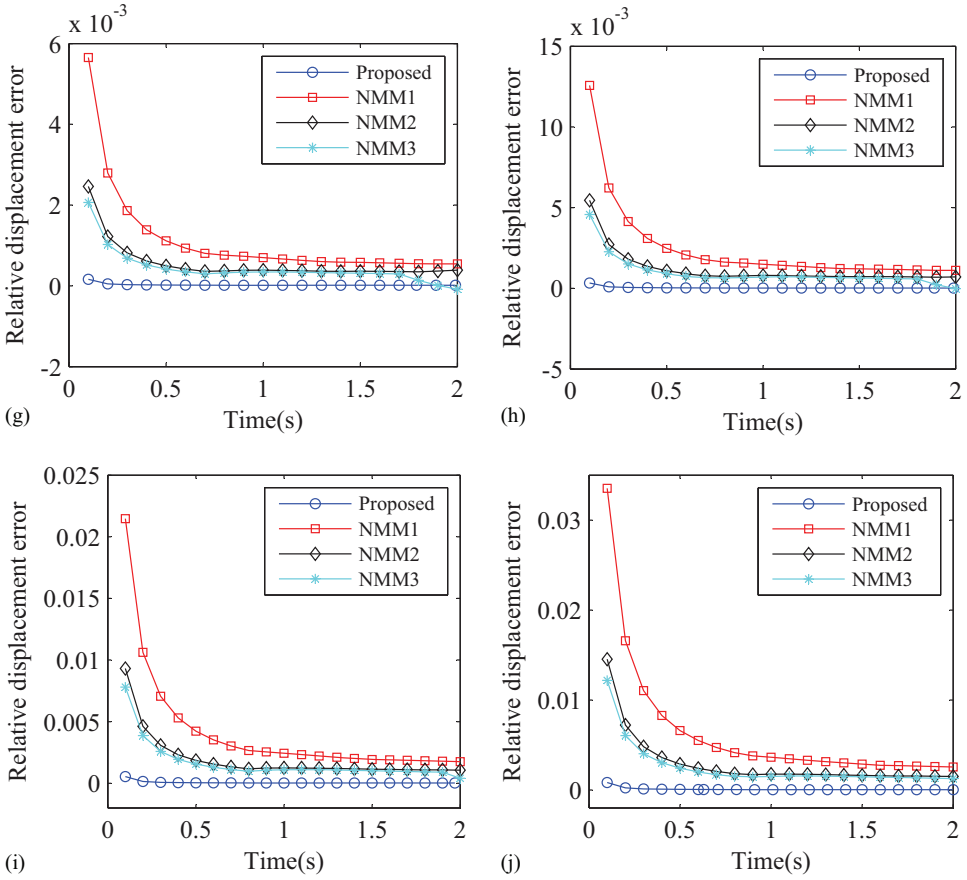

Fig. 10. (*Continued.*)

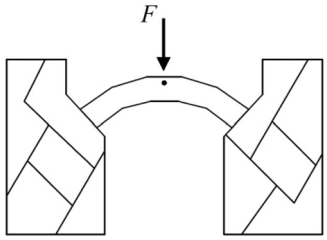

Fig. 11. Arch dam subjected to a point load F

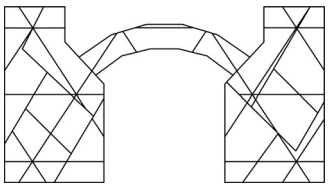

Fig. 12. Discrete model for the arch dam

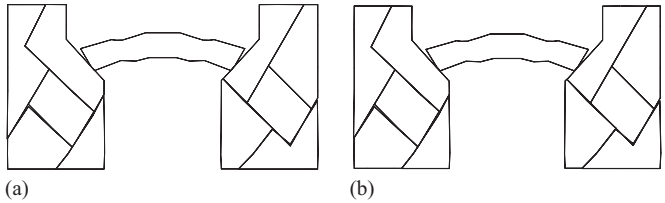

Fig. 13. Final deformation plots of the arch dam: (a) penalty method; (b) direct method

weight $\gamma = 0.5$, Young's modulus $E = 1.5$, and Poisson's ratio $\upsilon = 0.24$. Let the time step length $\Delta t = 0.01$ s and total computation time = 0.5 s.

The discrete model for this problem is shown in Fig. 12. The final deformation and principal stress plots obtained with the penalty method and direct approach are shown in Figs. 13–15. In addition, the displacement of the loading point versus the time is also plotted in Fig. 16. The results obtained with the proposed direct approach are very similar to those of penalty method.

Slope with Circular Sliding Surface

Fig. 17 shows a slope with a circular sliding surface. The left, right, and bottom boundaries of the model are all fixed. The sliding blocks and the slope have the same material parameters: Young's modulus $E = 5$ MPa, Poisson's ratio $\upsilon = 0.3$, density $\rho = 5 \times 10^3$ kg/m^3, and unit weight 5×10^4 kg/(m^{2}s^2). Let the time step length $\Delta t = 0.002$ s and total computation time = 0.202 s. The discrete model for this problem is shown in Fig. 18. The final deformation plots obtained with the penalty method and direct approach are shown in Fig. 19. In addition, the displacement of a character Point A versus the time is also plotted in Fig. 20. The result obtained with the proposed direct approach is very similar to that of the penalty method.

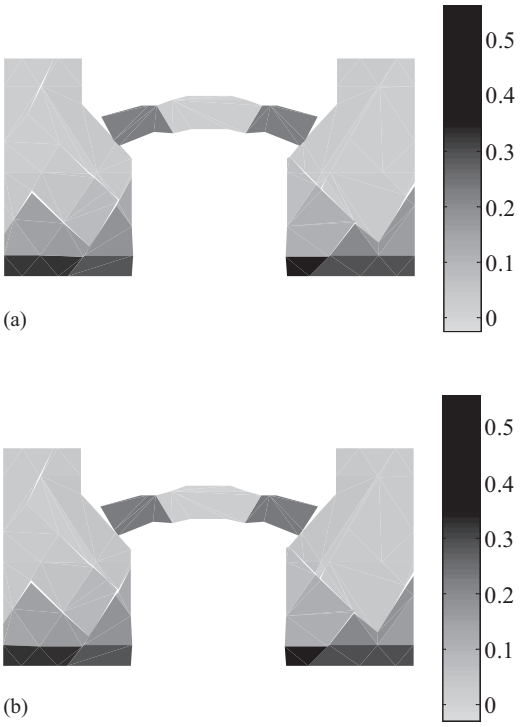

Fig. 14. Plots of the maximum principal stress (compressive stress is taken as positive): (a) penalty method; (b) direct method

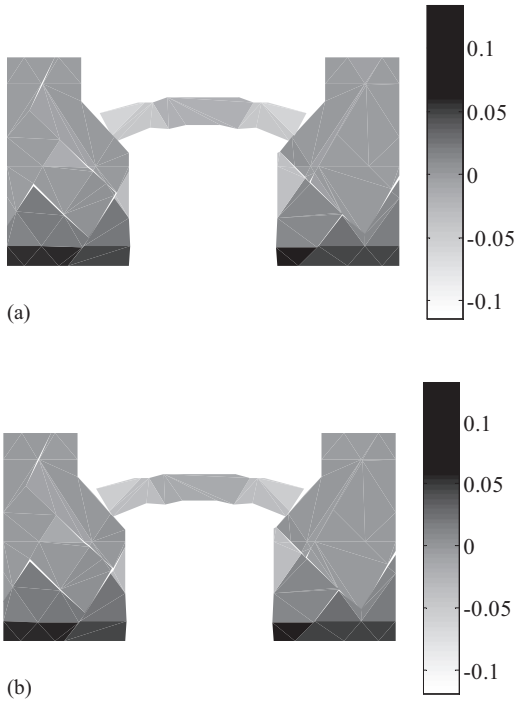

Fig. 15. Plots of the minor principal stress (compressive stress is taken as positive): (a) penalty method; (b) direct method

Layers of Thin Beams Subjected Point Load

Fig. 21 shows layers of stacking thin beams subjected to a point load. The bottom boundaries of the model are all fixed. The thin beams have the same material parameters: Young's modulus E = 10, Poisson's ratio $\upsilon = 0.24$, density $\rho = 0.3$, and unit weight –0.5.

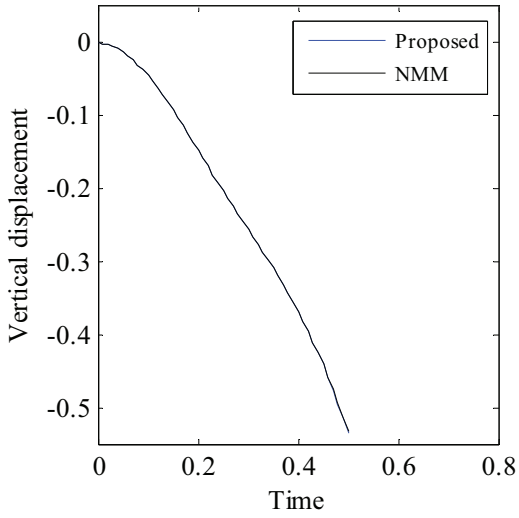

Fig. 16. Displacements of the measured point for the arch dam

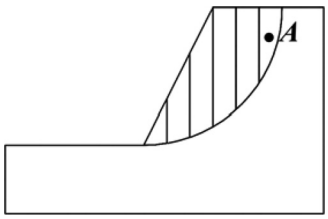

Fig. 17. Slope with circular sliding surface

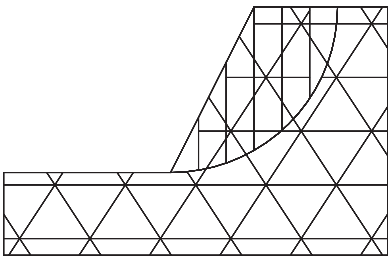

Fig. 18. Discrete model for the slope with circular sliding surface

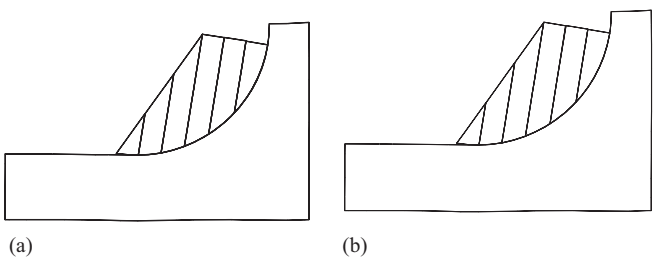

Fig. 19. Final deformation plots of the slope with circular sliding surface: (a) penalty method; (b) direct method

Let the time step length $\Delta t = 0.002$ and total computation time = 0.354. The final deformation and principal stress plots obtained with the proposed direct approach are shown in Figs. 22 and 23, respectively. The final deformation and stress distribution for this

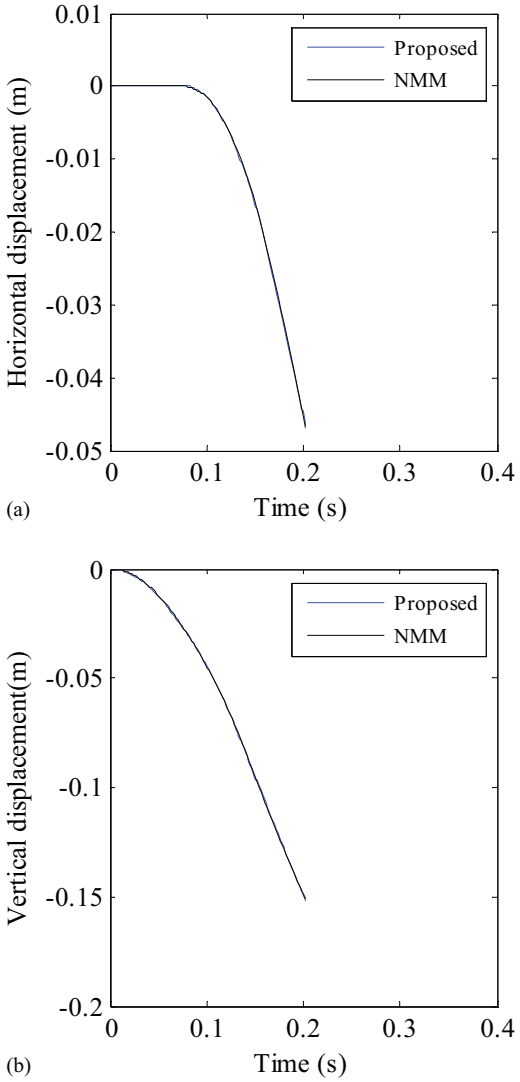

Fig. 20. Displacements of the measured point for the slope with circular sliding surface: (a) horizontal displacement; (b) vertical displacement

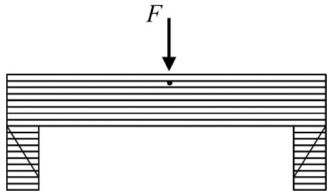

Fig. 21. Layers of thin beams subjected to a point load with $F = -1$

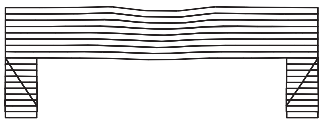

Fig. 22. Final deformation plot of the beams

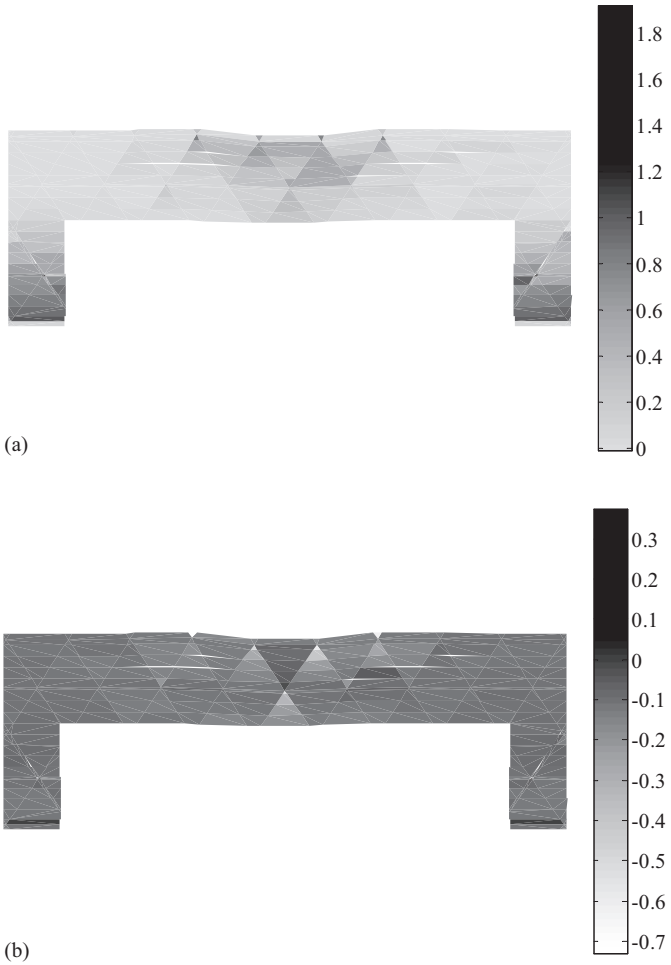

Fig. 23. Final principal stress plots of the beams (compressive stress is taken as positive): (a) the maximum principal stress; (b) the minor principal stress

symmetric structure is symmetrical, which could, to some extent, confirm the correctness of the proposed direct approach. In addition, the displacement of the loading point versus the time is also plotted in Fig. 24.

Conclusions

The performance of direct treatment of contact problems of NMM is investigated in the present work. The present method seems attractive for the following reasons:

1. Compared with the Lagrange multiplier method, the direct approach can solve out tangential contact forces directly by solving a nonsymmetric system. After a symmetrization treatment to the direct approach can derive a symmetrical system matrix, which could save storage space.
2. Compared with the penalty method, the proposed method has better accuracy. Moreover, it is free from the penalty parameter, which is very difficult to determine.
3. Implementation of the proposed method is easy, which could be achieved through very limited modification of the original NMM codes provided by Shi (1991).
4. The proposed direct approach could be applied in DDA without any handicap.

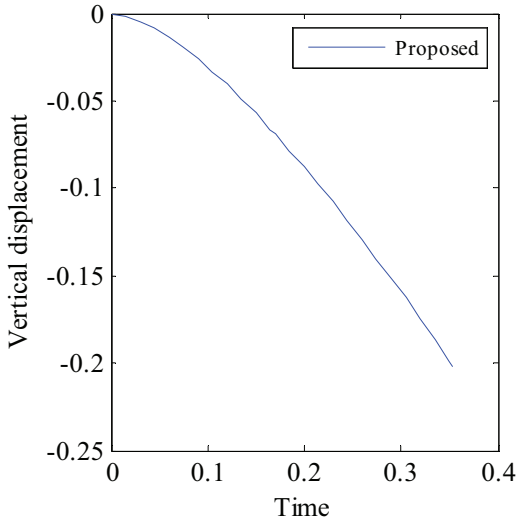

Fig. 24. Displacements of the measured point for the beams

Recently Shi (2015) proposed a 3D contact theory, which is a particularly exciting news. This theory will be fully utilized to extend the proposed method to its 3D version to solve more realistic engineering problems.

Although the proposed direct approach has more attractive advantages than the conventional penalty method, it introduces the contact force and increases the number of unknowns and consumes more memory space than the penalty method. If very complex engineering problems are involved, the contact pairs will be significantly increased, and the memory space consumption for the direct approach will be greater than the penalty method. As a result, more efficient solution algorithms are vital to solve those problems with a huge number of unknowns.

Acknowledgments

This study is supported by the National Basic Research Program of China (973 Program), under Grant No. 2014CB047100, and the National Natural Science Foundation of China, under Grant Nos. 11172313 and 51538001.

References

Areias, P., and Belytschko, T. (2005). "Analysis of three-dimensional crack initiation and propagation using the extended finite element method." *Int. J. Numer. Methods Eng.*, 63(5), 760–788.

Babuška, I., and Melenk, J. M. (1997). "The partition of unity method." *Int. J. Numer. Methods Eng.*, 40(4), 727–758.

Bao, H. R., Zhao, Z. Y., and Tian, Q. (2014). "On the Implementation of augmented Lagrangian method in the two-dimensional discontinuous deformation analysis." *Int. J. Numer. Anal. Methods Geomech.*, 38(6), 551–571.

Barla, M., Piovano, G., and Grasselli, G. (2012). "Rock slide simulation with the combined finite-discrete element method." *Int. J. Geomech.*, 10 .1061/(ASCE)GM.1943-5622.0000204, 711–721.

Belytschko, T., Krongauz, Y., Organ, D., Fleming, M., and Krysl, P. (1996). "Meshless methods: An overview and recent developments." *Comput. Methods Appl. Mech. Eng.*, 139(1–4), 3–47.

Beskos, D. E. (1987). "Boundary element methods in dynamic analysis." *Appl. Mech. Rev.*, 40(1), 1–23.

Beskos, D. E. (1997). "Boundary element methods in dynamic analysis: Part II (1986-1996)." *Appl. Mech. Rev.*, 50(3), 149–197.

Cai, Y. C., Zhuang, X. Y., and Zhu, H. H. (2013). "A generalized and efficient method for finite cover generation in the numerical manifold method." *Int. J. Comput. Methods*, 10(05), 1350028.

Cai, Y. G., He, T., and Wang, R. (2000). "Numerical simulation of dynamic process of the Tangshan earthquake by a new method-LDDA." *Pure Appl. Geophys*, 157(11), 2083–2104.

Chen, G. Q., Ohnishi, Y., and Ito, T. (1998). "Development of high-order manifold method." *Int. J. Numer. Methods Eng.*, 43(4), 685–712.

Cundall, P. A. (1971). "A computer model for simulating progressive, large-scale movements in blocky rock systems." *Proc., Symp. of the Int. Society of Rock Mechanics*, Nancy, France, Vol. 1, International Society for Rock Mechanics, Lisbon, Portugal, Paper II–8, 129–136.

Desai, C. S., Zaman, M. M., Lightner, J. G., Siriwardane, H. J. (1984). "Thin-layer element for interfaces and joints." *Int. J. Numer. Anal. Methods Geomech.*, 8(1), 19–43.

Dolbow, J., and Belytschko, T. (1999). "A finite element method for crack growth without remeshing." *Int. J. Numer. Methods Eng.*, 46(1), 131–150.

Doolin, D. M., and Sitar, N. (2004). "Time integration in discontinuous deformation analysis." *J. Eng. Mech.*, 10.1061/(ASCE)0733-9399(2004)130: 3(249), 249–258.

Duarte, C. A., Hamzeh, O. N., Liszka, T. J., and Tworzydlo, W. W. (2001). "A generalized finite element method for the simulation of three-dimensional dynamic crack propagation." *Comput. Methods Appl. Mech. Eng.*, 190(15), 2227–2262.

Goodman, R. E., and John, S. (1977). "Finite element analysis for discontinuous rocks." *Numerical methods in geotechnical engineering*, C. S. Desai and J. T. Christian, eds., McGraw-Hill Book, New York, 148–175.

He, L., An, X. M., Ma, G. W., and Zhao, Z. Y. (2013). "Development of three-dimensional numerical manifold method for jointed rock slope stability analysis." *Int. J. Rock Mech. Min. Sci.*, 64, 22–35.

He, L., An, X. M., and Zhao, Z. Y. (2014). "Development of contact algorithm for three-dimensional numerical manifold method." *Int. J. Numer. Methods Eng.*, 97(6), 423–453.

He, L., and Ma, G. W. (2010). "Development of 3D numerical manifold method." *Int. J. Comput. Methods*, 7, 107–129.

Jiang, Q. H., Chen, Y. F., Zhou, C. B., and Yeung, M. R. (2013). "Kinetic energy dissipation and convergence criterion of discontinuous deformations analysis (DDA) for geotechnical engineering." *Rock Mech. Rock Eng.*, 46(6), 1443–1460.

Jiang, Q. H., Deng, S. S., Zhou, C. B., and Lu, W. B. (2010). "Modeling unconfined seepage flow using three-dimensional numerical manifold method." *J. Hydrodyn.*, 22(4), 554–561.

Jiang, Q. H., Zhou, C. B., and Li, D. Q. (2009). "A three-dimensional numerical manifold method based on tetrahedral meshes." *Comput. Struct.*, 87(13–14), 880–889.

Jiang, W., and Zheng, H. (2011). "Discontinuous deformation analysis based on variational inequality theory." *Int. J. Comput. Methods*, 8(2), 193–208.

Jing, L. (2003). "A review of techniques, advances and outstanding issues in numerical modelling for rock mechanics and rock engineering." *Int. J. Rock Mech. Min. Sci.*, 40(3), 283–353.

Lin, C. T., Amadei, B., Jung, J., Dwyer, J. (1996). "Extensions of discontinuous deformation analysis for jointed rock masses." *Int. J. Rock Mech. Min. Sci.*, 33(7), 671–694.

Katona, M. G. (1983). "A simple contact–friction interface element with applications to buried culverts." *Int. J. Numer. Anal. Methods Geomech.*, 7(3), 371–384.

Ma, G., Zhou, W., Chang, X. and Yuan, W. (2014). "Combined FEM/DEM modeling of triaxial compression tests for rockfills with polyhedral particles." *Int. J. Geomech.*, 10.1061/(ASCE)GM.1943-5622.0000372, 04014014.

Ma, G. W., An, X. M., and He, L. (2010). "The numerical manifold method: A review." *Int. J. Comput. Methods*, 7(1), 1–32.

Munjiza, A. (2004). *The combined finite-discrete element method*, John Wiley & Sons, New York.

Ning, Y. J., An, X. M., and Ma, G. W. (2011). "Footwall slope stability analysis with the numerical manifold method." *Int. J. Rock Mech. Min. Sci.*, 48(6), 964–975.

Perrone, N., and Kao, R. (1975). "A general finite difference method for arbitrary meshes." *Comput. Struct.*, 5(1), 45–57.
Rabczuk, T., and Belytschko, T. (2004). "Cracking particles: a simplified mesh-free method for arbitrary evolving cracks." *Int. J. Numer. Methods Eng.*, 61(13), 2316–2343.
Reddy, J. N. (2004). *An introduction to nonlinear finite element analysis*, Oxford University Press, Oxford, U.K.
Shi, G. H. (1988). "Discontinuous deformation analysis: A new numerical model for the statics and dynamics of block systems." Ph.D. thesis, Dept. of Civil Engineering, Univ. of California, Berkeley, CA.
Shi, G. H. (1991). "Manifold method of material analysis." *Transactions of the 9th Army Conf. on Applied Mathematics and Computing, Rep. No. 92-1*, U.S. Army Research Office, Minneapolis, MN, 57–76.
Shi, G. H. (2015). "Contact theory." *Sci. China Ser. E.*, 58(9), 1450–1496.
Simo, J. C., and Laursen, T. A. (1992). "An augmented Lagrangian treatment of contact problems involving friction." *Comput. Struct.*, 42(1), 97–116.
Spivak, M. (1965). *Calculus on manifolds: A modern approach to classical theorems of advanced calculus*, W. A. Benjamin, New York.
Strouboulis, T., Babuška, I., and Copps, K. (2000). "The design and analysis of the generalized finite element method." *Comput. Methods Appl. Mech. Eng.*, 181(1), 43–69.
Stupkiewicz, S., Lengiewicz, J., and Korelc, J. (2010). "Sensitivity analysis for frictional contact problems in the augmented Lagrangian formulation." *Comput. Methods Appl. Mech. Eng.*, 199(33–36), 2165–2176.
Sun, L., Zhao, G. F., and Zhao, J. (2013). "Particle manifold method (PMM): A new continuum-discontinuum numerical model for geomechanics." *Int. J. Numer. Anal. Methods Geomech.*, 37(12), 1711–1736.
Wei, W., Jiang, Q., and Peng, J. (2016). "New rock bolt model and numerical implementation in numerical manifold method." *Int. J. Geomech.*, 10.1061/(ASCE)GM.1943-5622.0000669, E4016004.
Wong, L. N. Y., and Wu, Z. (2014). "Application of the numerical manifold method to model progressive failure in rock slopes." *Eng. Fract. Mech.*, 119, 1–20.
Yan, C. Z., Zheng, H., Sun, G. H., and Ge, X. R. (2016). "Combined finite-discrete element method for simulation of hydraulic fracturing." *Rock Mech. Rock Eng*, 49(4), 1389–1410.
Yang, Y. T., Xu, D. D., and Zheng, H. (2014). "Evaluation on stress intensity factor of crack under dynamic load using numerical manifold method." *Chin. J. Theor. Appl. Mech.*, 46, 730–738.
Zhang, G. X., Zhao, Y., and Peng, X. C. (2010). "Simulation of toppling failure of rock slope by numerical manifold method." *Int. J. Comput. Methods*, 7(1), 167–189.
Zheng, H., and Jiang, W. (2009). "Discontinuous deformation analysis based on complementary theory." *Sci. China Ser. E.*, 52(9), 2547–2554.
Zheng, H., and Li, J. L. (2007). "A practical solution for KKT systems." *Numer. Algorithms*, 46(2), 105–119.
Zheng, H., and Li, X. K. (2015a). "Mixed linear complementarity formulation of discontinuous deformation analysis." *Int. J. Rock Mech. Min. Sci.*, 75, 23–32.
Zheng, H., Liu, D. F., Lee, C. F., and Yue, Z. Q. (2004). "A sophisticated node-pair model for interface problems." *Comput. Geotech.*, 31(2), 137–153.
Zheng, H., Liu, F., and Du, X. L. (2015b). "Complementarity problem arising from static growth of multiple cracks and MLS-based numerical manifold method." *Comput. Methods Appl. Mech. Eng.*, 295, 150–171.
Zheng, H., Liu, F., and Li, C. (2014a). "The MLS-based numerical manifold method with applications to crack analysis." *Int. J. Fract.*, 190(1–2), 147–166.
Zheng, H., Liu, F., and Li, C. (2015c). "Primal mixed solution to unconfined seepage flow in porous media with numerical manifold method." *Appl. Math. Model.*, 39(2), 794–808.
Zheng, H., Liu, Z. J., and Ge, X. R. (2013). "Numerical manifold space of Hermitian form and application to Kirchhoff's thin plate problems." *Int. J. Numer. Methods Eng.*, 95(9), 721–739.
Zheng, H., and Xu, D. D. (2014b). "New strategies for some issues of numerical manifold method in simulation of crack propagation." *Int. J. Numer. Methods Eng.*, 97(13), 986–1010.
Zheng, H., Zhang, P., and Du, X. L. (2016). "Dual form of discontinuous deformation analysis." *Comput. Methods Appl. Mech. Eng.*, 305, 196–216.
Zienkiewicz, O. C., and Taylor, R. L. (2000). *The finite element method*, 5th Ed., Butterworth-Heinemann, Oxford, U.K.